Hyperspectral Imagery Denoising Based on Oblique Subspace Projection

Qian Wang, Lifu Zhang, *Member, IEEE,* Qingxi Tong, and Feizhou Zhang

***Abstract*—This paper presents a hyperspectral imagery denoising algorithm based on oblique subspace projection (DOBSP), which considers the correlation between noise and signal. The algorithm first estimates the signal and noise through segmentation Gaussian filtering which can reduce more influence of the image texture than traditional Gaussian filtering. Then, signal and noise estimates are fed into principal component analysis (PCA) to identify their respective subspace basis vectors. Finally, these basis vectors are used to compute matrices of oblique subspace projection (OBSP), and the signal and noise are extracted from the original image through OBSP. We assessed the DOBSP algorithm using both simulated and real Hyperion images. The orthogonal subspace projection (OSP) which assumes that noise is independent on signal and the subspace-based striping noise reduction (SBSR) algorithm which uses polynomial model to describe the relationship between noise and signal were introduced for comparison. Compared with signal and noise results by OSP and SBSR, both signal and noise extracted by DOBSP on the simulated image are closer to the original simulated signal and noise, and the noise image obtained by DOBSP on the Hyperion image has fewer textures.**

***Index Terms*—Denoising, hyperspectral image, oblique subspace projection (OBSP), orthogonal subspace projection (OSP).**

I. Introduction

HYPERSPECTRAL imaging is a key technique for observing the Earth through traditional two-dimensional imaging remote sensing technology and spectroscopy [1]–[3]. It simultaneously obtains geo- and radiometric information as well as abundant spectral information [4]. However, this useful information is often contaminated by the noise, crippling its application. Hence, denoising is an important part of hyperspectral image processing [5]–[10].

The noise of hyperspectral images is present in both time and spatial domains [11]. The time-domain noise is related to each pixel of the detector. As a common example of time-domain noise, shot noise is introduced by light current from target and nontarget radiation, and by dark current. The relation between shot noise and target radiation demonstrates that shot noise is partly correlated with the signal in an image. Different from time-domain noise, spatial-domain noise is caused by the use of multielement and focal plane detectors. For a hyperspectral image, its spatial-domain noise, which is usually manifested as striping noise, can be introduced by nonuniformity in the detector response. This type of noise is modeled as the multiplication of the detector's nonuniformity parameter and the image's average value [11]. The image's average value is mainly dependent on the signal. Thus the striping noise relates to the signal. From the above analysis about the noise's generation mechanism, both time-domain and spatial-domain noises of the hyperspectral image are related to its signal. Hence, the noise subspace is not necessarily orthogonal to the signal subspace. Methods based on orthogonal subspace projection (OSP) [12]–[15] such as principal component analysis (PCA) [16]–[22] and minimum noise fraction (MNF) [23]–[25], which omit the correlation between the noise and signal, are not accurate. In addition, the hyperspectral signal from adjacent bands is highly relevant, and the noise is related to the signal in each band according to the noise's generation mechanism. Hence, the relevance may exist in the noise from adjacent bands, and the covariance matrix of the noise data may not be diagonal. Therefore, the correlation between the noise and signal should be taken into account in the denoising procedure.

The dependence of noise on signal has been taken into consideration in some recent studies. Selva *et al.* [26], [27] presented a generalized signal-dependent noise (GSD) model that relies on the multivariate regression of local sample statistics such as mean and variance. It can only obtain the variance of the noise, not the whole noise image. The GSD model assumes that the noise is composed of GSD regarded as a regression function of the noise-free image, and electronics noise independent of the signal. Actually, the electronic noise is not always independent of the signal due to the time-domain noise's generation reason. Acito *et al.* [28], [29] thought the striping noise is dependent on the signal and proposed the subspace-based striping noise reduction (SBSR) algorithm to reduce the striping noise and time-domain noise in the hyperspectral image. The relationship between the noise and signal is modeled as a polynomial function of the signal level. But the order of the polynomial is empirical and not unique. Moreover, the noise is estimated based on the assumption that the noise subspace is orthogonal to the signal subspace in SBSR. For the original image $\mathbf{X}$, $\mathbf{P}_S$ denotes the

Manuscript received November 28, 2013; revised March 23, 2014; accepted June 01, 2014. Date of publication June 30, 2014; date of current version August 01, 2014. This research was supported in part by the National Natural Science Foundation of China under Grant 41371362, Grant 41272364, and Grant 41201348 and in part by the National High-Technology Research and Development Program of China (863 Program) under Grant 2012AA12A301. *(Corresponding author: Feizhou Zhang.)*

Q. Wang is with the State Key Laboratory of Remote Sensing Science, Institute of Remote Sensing and Digital Earth, Chinese Academy of Sciences, 100101 Beijing, China, and also with the University of Chinese Academy of Sciences, 100049 Beijing, China (e-mail: wangqian12031@163.com).

L. Zhang and Q. Tong are with the State Key Laboratory of Remote Sensing Science, Institute of Remote Sensing and Digital Earth, Chinese Academy of Sciences, 100101 Beijing, China (e-mail: zhanglf@radi.ac.cn; tqxi@263.net).

F. Zhang is with the School of Earth and Space Sciences, Peking University, 100871 Beijing, China (e-mail: zhangfz@pku.edu.cn).

Color versions of one or more of the figures in this paper are available online at http://ieeexplore.ieee.org.

Digital Object Identifier 10.1109/JSTARS.2014.2329322

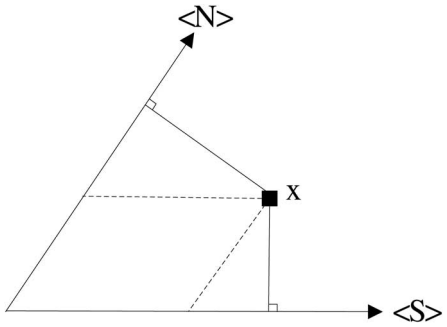

Fig. 1. Diagrams of OBSP (dash line) and OSP (solid line). x is the original pixel; $<\mathrm{S}>$ and $<\mathrm{N}>$ represent signal subspace and noise subspace, respectively.

projection matrix on the signal subspace, and $\mathbf{P}_S^{\perp}$ is the projection matrix on the orthogonal complement of the signal subspace. In SBSR algorithm, the signal and noise are estimated respectively by OSP as

$$\hat{\mathbf{S}} = \mathbf{P}_s \mathbf{X} \tag{1}$$

and

$$\hat{\mathbf{N}} = \mathbf{P}_s^{\perp} \mathbf{X}. \tag{2}$$

Thus the noise estimate is uncorrelated with the signal estimate. The noise $R_l(i, j, S_l(i, j))$ at the ith column jth line of the lth band is related to the signal $S_l(i, j)$ at the corresponding location

$$R_l(i, j, S_l(i, j)) = \sum_{r=0}^{N} A_l^{(r)}(i) \bullet \hat{S}_l^{(r)}(i, j). \tag{3}$$

The polynomial coefficients

$$\left\{A_l^{(r)}(i)\right\}_{r=0}^{N} = \arg\min \sum_{j=1}^{N_L} \left| \hat{N}_l(i, j, \hat{S}_l(i, j)) - \sum_{r=0}^{N} A_l^{(r)}(i) \cdot \hat{S}_l^{(r)}(i, j) \right|^2 \tag{4}$$

where r indicates the order of the polynomial. In essence, both the GSD model and SBSR model belong to the polynomial model. Although the polynomial model considers dependence of noise on signal, it is empirical and lacks strict physical proofs.

According to the noise's generation mechanism, the noise is dependent on the signal. Hence the denoising method with OSP, which is based on the assumption that the noise is independent on the signal, is problematic. Moreover, the polynomial model used to describe the relation between the noise and signal is also based on an assumption without effective proofs. In this paper, we present a new denoising algorithm based on oblique subspace projection (DOBSP). The oblique subspace projection (OBSP) regards the signal subspace and noise subspace as oblique, considering the correlation between the noise and signal. Fig. 1 shows the diagrams of OBSP and OSP. When noise is correlated with signal, noise subspace is oblique with signal subspace. The signal result with projecting the original image into signal subspace along noise subspace is more accurate than that with projecting the original image into signal subspace orthogonally. Likewise, projecting the original image into noise subspace along signal subspace obtains a better noise result than projecting the original image into noise subspace orthogonally. Hence, the

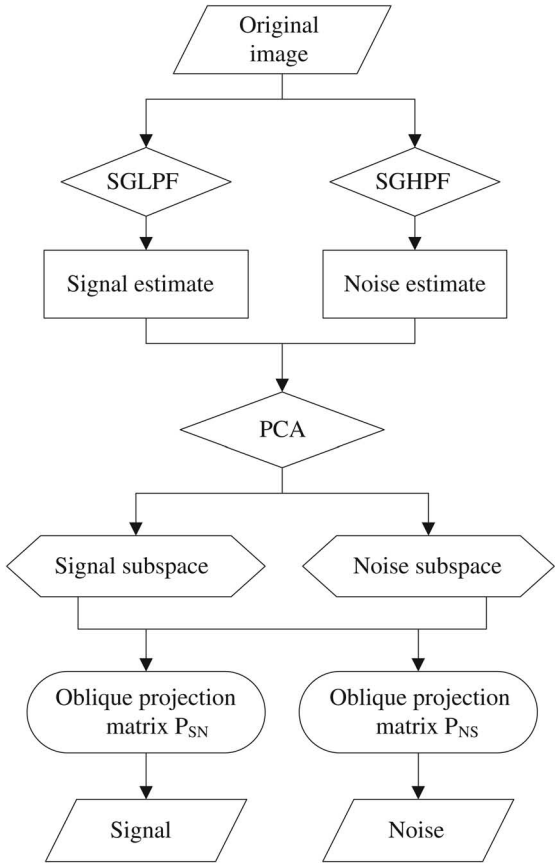

Fig. 2. Overall process of the DOBSP.

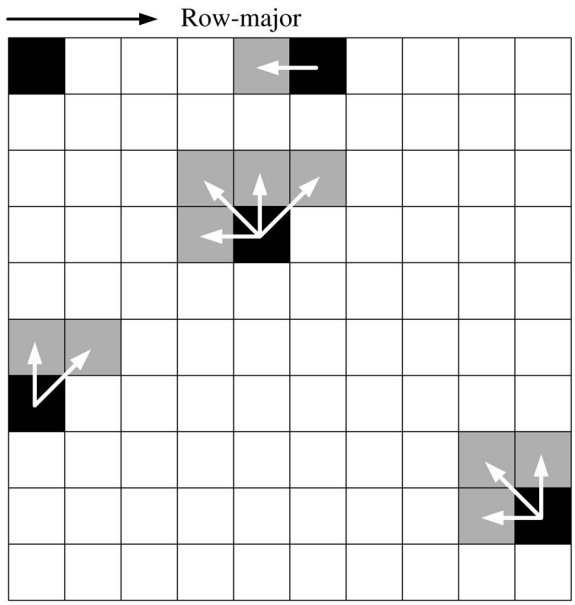

Fig. 3. Traversal sequence of image pixels [6], [9].

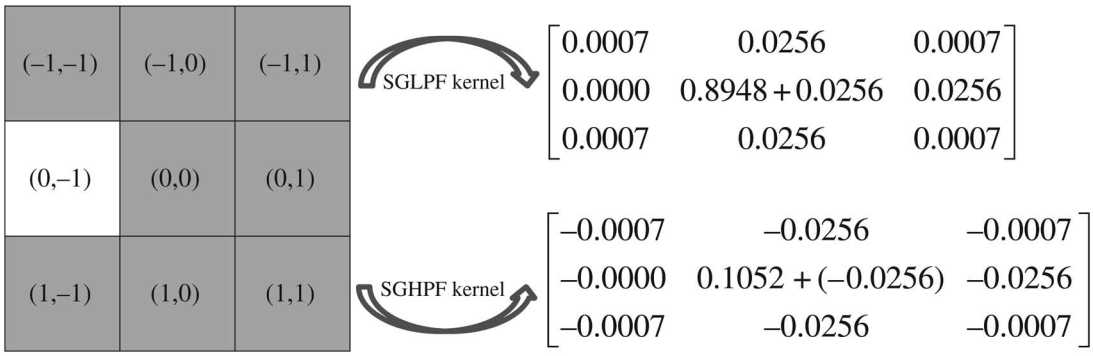

Fig. 4. Kernel adjustment for irregular blocks in segmentation Gaussian filtering. The squares filled with gray and white represent two different ground objects.

OBSP is more effective and sensible than the OSP when the noise is dependent on the signal. In DOBSP algorithm, identifying signal and noise subspaces accurately is crucial. The paper proposes a segmentation Gaussian filtering method, which can reduce more influence of the image texture than traditional Gaussian filtering, to estimate the signal and noise, respectively, from the original image. The image texture is caused by the spectral difference of various ground objects, especially referring to the boundary between different adjacent ground objects in the paper. Then PCA is applied to the signal and noise estimates to get their respective eigenvectors, which are selectively used to build their respective subspaces. In addition, simulated and real Hyperion images are used as experimental data to assess the DOBSP algorithm.

II. Algorithm and Data

A. Image Model

The original image's whole space $\boldsymbol{V}$ can be decomposed to the signal subspace $\boldsymbol{V}_S$ and noise subspace $\boldsymbol{V}_N$

$$\boldsymbol{V} = \boldsymbol{V}_S \oplus \boldsymbol{V}_N. \tag{5}$$

$\oplus$ indicates the direct sum. The signal subspace and noise subspace may be orthogonal or oblique. For the original image data $\mathbf{X} = [\,\boldsymbol{x}_1 \quad \boldsymbol{x}_2 \quad \cdots \quad \boldsymbol{x}_N\,]$

$$\boldsymbol{x}_i = \boldsymbol{s}_i^* + \boldsymbol{n}_i^* \tag{6}$$

where $\boldsymbol{x}_i \in \boldsymbol{V}$, $\boldsymbol{s}_i^* \in \boldsymbol{V}_S$, and $\boldsymbol{n}_i^* \in \boldsymbol{V}_N$. $\boldsymbol{x}_i$ is a $L \times 1$ vector of the ith pixel, $i = 1, 2, \ldots, N$. N is the number of pixels, and L is the number of bands. The addition of vectors $\boldsymbol{s}_i^*$ and $\boldsymbol{n}_i^*$ obeys the parallelogram rule.

Then, transform $\boldsymbol{s}_i^*$ and $\boldsymbol{n}_i^*$ from signal subspace $\boldsymbol{V}_S$ and noise subspace $\boldsymbol{V}_N$ into image space $\boldsymbol{V}$, and obtain

$$\boldsymbol{s}_i = \mathbf{P}_{SN}\boldsymbol{x}_i \tag{7}$$

and

$$\boldsymbol{n}_i = \mathbf{P}_{NS}\boldsymbol{x}_i \tag{8}$$

where $\boldsymbol{s}_i \in \boldsymbol{V}$, $\boldsymbol{n}_i \in \boldsymbol{V}$. $\mathbf{P}_{SN}$ and $\mathbf{P}_{NS}$ are two OBSP matrices. $\mathbf{P}_{SN}$ is the projection matrix on signal subspace along noise subspace, while $\mathbf{P}_{NS}$ is the projection matrix on noise subspace along signal subspace. Thus

$$\boldsymbol{s}_i + \boldsymbol{n}_i = (\mathbf{P}_{SN} + \mathbf{P}_{NS})\boldsymbol{x}_i. \tag{9}$$

Because vectors $\boldsymbol{s}_i$ and $\boldsymbol{n}_i$ lie in the same space $\boldsymbol{V}$, the addition of $\boldsymbol{s}_i$ and $\boldsymbol{n}_i$ obeys the common matrix addition rule. If $\mathbf{P}_{SN} + \mathbf{P}_{NS} = \mathbf{I}$ ($\mathbf{I}$ is the identity matrix), the noise subspace is orthogonal to the signal subspace

$$\boldsymbol{x}_i = \boldsymbol{s}_i + \boldsymbol{n}_i. \tag{10}$$

Otherwise

$$\boldsymbol{x}_i = (\mathbf{P}_{SN} + \mathbf{P}_{NS})^{-1}(\boldsymbol{s}_i + \boldsymbol{n}_i) \tag{11}$$

where the result of $\mathbf{P}_{SN} + \mathbf{P}_{NS}$ should be nonsingular. Equation (11) can also be written in matrix form as

$$\mathbf{X} = (\mathbf{P}_{SN} + \mathbf{P}_{NS})^{-1}(\mathbf{S} + \mathbf{N}). \tag{12}$$

B. DOBSP Algorithm

The DOBSP algorithm has been briefly introduced in Section I. This algorithm mainly consists of the following three steps. First, the segmentation Gaussian filtering, which can reduce more effects of the image texture than traditional Gaussian filtering, is applied to the original image. Thus the signal and noise are estimated respectively. Secondly, the signal and noise estimates are fed into PCA to identify their respective subspace basis vectors. Finally, the oblique projection matrices $\mathbf{P}_{SN}$ and $\mathbf{P}_{NS}$ are computed based on basis vectors of the two subspaces. The overall process of the DOBSP is shown in Fig. 2. The implementation of the above three steps will be described in detail in Sections II-B1–II-B3.

1) Signal and Noise Estimation: Gaussian filtering is an information–extraction method [30]. Gaussian low-pass filtering (GLPF) retains low-frequency information as the signal, while Gaussian high-pass filtering (GHPF) extracts high-frequency information as the noise. The GLPF uses the Gaussian function

$$y = e^{-x^2/2\sigma^2} \tag{13}$$

for weighting, where x denotes the distance between adjacent pixels and target pixel. σ is the standard deviation, and y is the

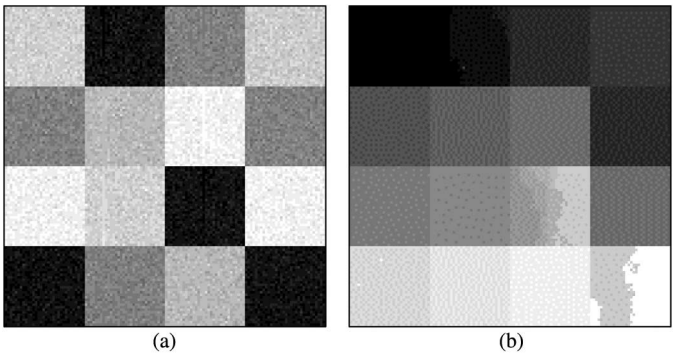

Fig. 5. Band 200 (914.0 nm) of the simulated image (a) and its segmented result (b).

weight of the adjacent pixel [30]. The weighted function for GHPF is

$$y = 1 - e^{-x^2/2\sigma^2}. \tag{14}$$

The Gaussian function is characterized by rotational symmetry, with weight's absolute value decreasing with distance from target pixel increasing. These characteristics allow GLPF (GHPF) to preserve (omit) some textures. Inevitably, some textures will be smoothened by GLPF, while some textures may be highlighted by GHPF. This shortcoming will affect the accuracy of the signal and noise estimates.

To overcome this shortcoming, we replace the traditional Gaussian filtering with segmentation Gaussian filtering. The signal is estimated by segmentation Gaussian low-pass filtering (SGLPF) and noise by segmentation Gaussian high-pass filtering (SGHPF). The segmentation Gaussian filtering consists of the following two steps.

Firstly, the original image is segmented into homogeneous or quasi-homogeneous blocks with a small spectral angle threshold, based on the spatial distribution continuity of ground objects. The adjacent two pixels whose spectral angle is smaller than the threshold belong to one same block. The specific process of image segmentation is shown in Fig. 3. Pixels are traversed successively in row-major order. For each pixel awaiting segmentation (filled with black), the spectral angle between it and each previous pixel (filled with gray) which has been traversed will be computed. The awaiting pixel belongs to the same block as the pixel whose spectral angle with the awaiting pixel is minimum.

Then, each block is processed with Gaussian filtering. This study chooses the widely used 3×3 kernels

$$\begin{bmatrix} 0.0007 & 0.0256 & 0.0007 \\ 0.0256 & 0.8948 & 0.0256 \\ 0.0007 & 0.0256 & 0.0007 \end{bmatrix}$$

and

$$\begin{bmatrix} -0.0007 & -0.0256 & -0.0007 \\ -0.0256 & 0.1052 & -0.0256 \\ -0.0007 & -0.0256 & -0.0007 \end{bmatrix}$$

for the SGLPF and SGHPF, respectively [31]. However, the ground object's spatial shape is usually irregular, thus the block corresponding to this ground object is also not square. Hence, a certain adjacent pixel covered by a kernel may belong to a different block from the target pixel. In this case, the weight of that adjacent pixel is added to the weight of the target pixel, and that adjacent pixel's weight is set to 0 (Fig. 4). This adjustment for kernel avoids distortion of the pixel value. Through the segmentation Gaussian filtering, the texture formed by

TABLE I
HYPERION BANDS USED IN THE EXPERIMENT

Optical head	Band number	Wavelength (nm)
VNIR	13–54	478–895
SWIR	83–97	973–1114
	99–118	1134–1326
	135–164	1498–1790
	193–199	2083–2243

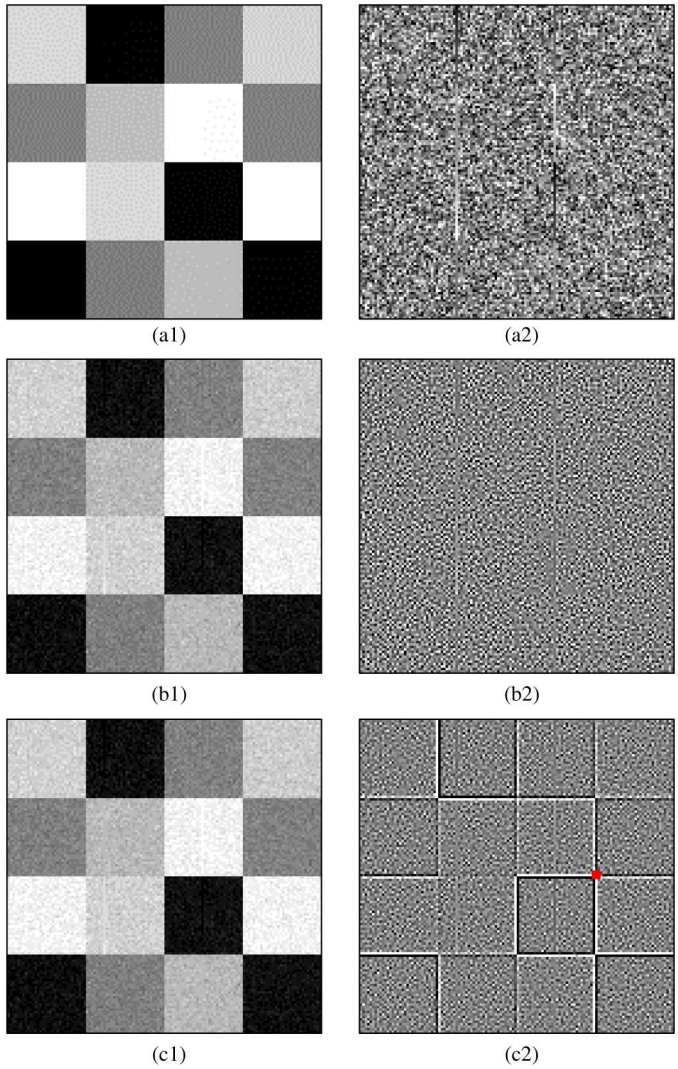

Fig. 6. Band 200 (914.0 nm) of the signal and noise estimates. (a1) Simulated signal. (a2) Simulated noise. (b1) Signal estimated by SGLPF. (b2) Noise estimated by SGHPF. (c1) Signal estimated by GLPF. (c2) Noise estimated by GHPF and the red square indicates the location of the boundary pixel at line 64 and column 96.

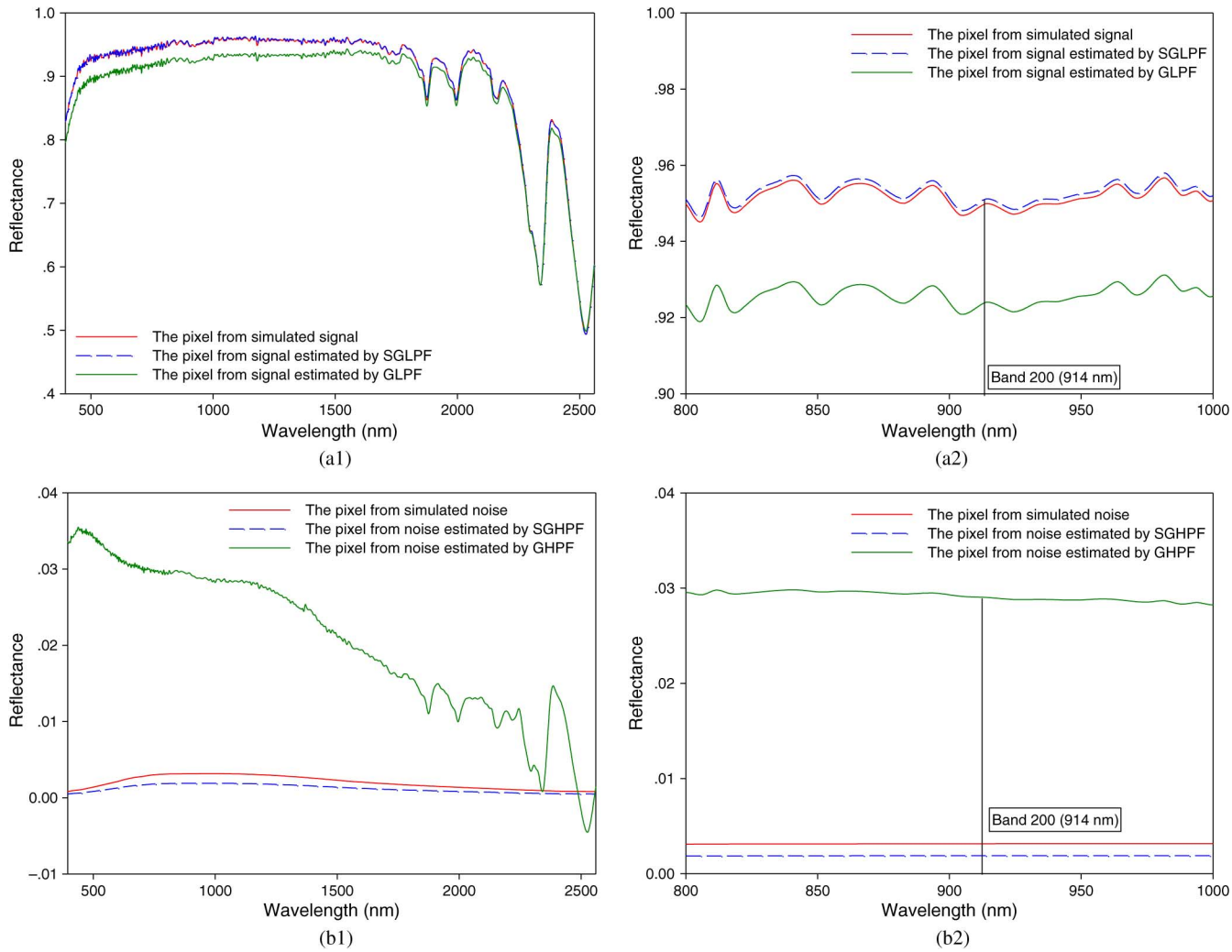

Fig. 7. Spectral curve of the boundary pixel at line 64 and column 96 from the signal and noise estimates. (a1) For signal estimate. (a2) Partial enlargement of (a1). (b1) For noise estimate. (b2) Partial enlargement of (b1).

neighboring blocks is reserved in signal estimate and omitted in noise estimate.

2) Subspace Identification: The purpose of subspace identification is to obtain the basis vector representing the subspace. The basis vector is selected from the eigenvector after PCA on image data by supervised method. The eigenvalue and eigenvector of signal covariance matrix were computed through PCA on signal estimate, while noise covariance matrix's eigenvalues and eigenvectors were computed through PCA on noise estimate [32]–[34]. It is worth mentioning that noise's covariance matrix is diagonal if noise from different bands is uncorrelated. Generally, several leading components of the signal estimate after PCA represent the signal information. The corresponding eigenvectors were chosen as the basis vectors of signal subspace. If there is some signal included in the noise estimate, the leading component probably contains the signal information. The basis vector of noise subspace can be chosen by visual inspecting noise's principal component images.

3) OBSP Matrix Computation: From the subspaces of the signal and noise estimates, the relevance between the noise and signal can be expressed using subspace angle [35], [36], with smaller than 90° denoting that noise subspace is oblique to signal subspace. Mathematically, the OSP can be treated as a special case of OBSP when the space angle between the signal and noise subspaces is 90°. Because the noise is usually correlated to signal, their subspace angle can deviate from 90°.

There are two transformation matrices involved in OBSP, the oblique projection matrix $\mathbf{P}_{SN}$, which projects the original image onto the signal subspace along the noise subspace, and $\mathbf{P}_{NS}$, which projects the original image onto the noise subspace along the signal subspace. We take $\mathbf{P}_{SN}$ as an example to illustrate how to compute the oblique projection matrix. The projection matrix of the signal subspace is

$$\mathbf{S}_{project} = \mathbf{S}_{basis}\mathbf{S}^{\#}_{basis} \tag{15}$$

where $\mathbf{S}_{basis}$ is the basis vector of the signal subspace and $\mathbf{S}^{\#}_{basis}$ is the generalized inverse matrix of $\mathbf{S}_{basis}$ [37]

$$\mathbf{S}^{\#}_{basis} = (\mathbf{S}_{basis}{}^{\mathrm{T}}\mathbf{S}_{basis})^{-1}\mathbf{S}_{basis}{}^{\mathrm{T}}. \tag{16}$$

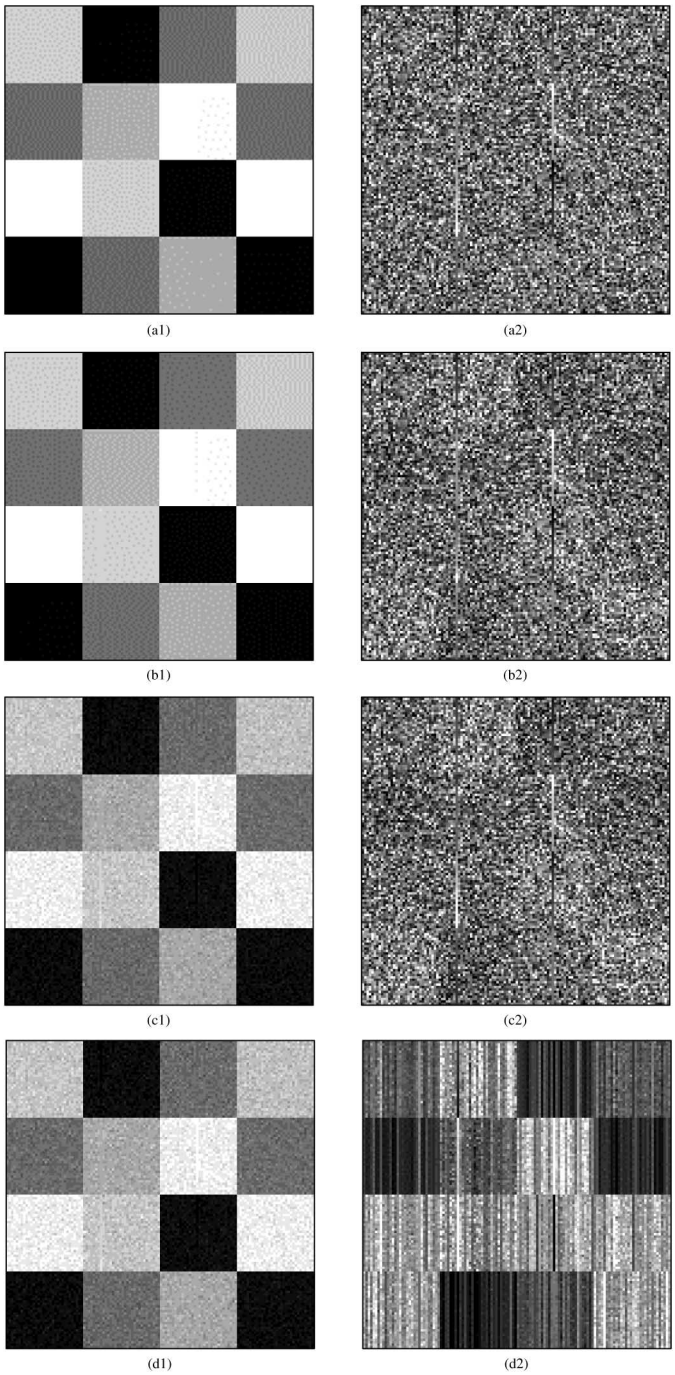

Fig. 8. Band 200 (914.0 nm) of the signal and noise results. (a1) Simulated signal. (a2) Simulated noise. (b1) Signal result by DOBSP. (b2) Noise result by DOBSP. (c1) Signal result by OSP. (c2) Noise result by OSP. (d1) Signal result by SBSR. (d2) Noise result by SBSR.

The orthogonal complement projection matrix of the signal subspace is

$$\mathbf{S}_{orthproject} = \mathbf{I} - \mathbf{S}_{project} \tag{17}$$

where $\mathbf{I}$ is the identity matrix. The orthogonal projection matrix of the noise subspace $\mathbf{N}_{orthproject}$ can be computed in the similar way. Then, $\mathbf{P}_{SN}$ is obtained as [38], [39]

$$\mathbf{P}_{SN} = \mathbf{S}_{basis}(\mathbf{S}_{basis}{}^{\mathrm{T}}\mathbf{N}_{orthproject}\mathbf{S}_{basis})^{-1}\mathbf{S}_{basis}{}^{\mathrm{T}}\mathbf{N}_{orthproject}. \tag{18}$$

The corresponding signal result is

$$\mathbf{S} = \mathbf{P}_{SN}\mathbf{X} \tag{19}$$

where $\mathbf{X}$ is the original image. Similarly, we can compute $\mathbf{P}_{NS}$ and get the noise result $\mathbf{N}$.

C. Experimental Data

Both simulated and real images were used in experiments to assess the DOBSP algorithm. Five types of minerals' spectrums (Alunite, Andradite, Calcite, Chlorite, and Kaolinite) from the United States Geological Surve (USGS) spectral library were chosen to generate the simulated signal. The simulated signal data set has 420 bands and 128 samples of 128 lines. There are 16 ground objects corresponding to 16 (4×4) obvious blocks in the simulated signal [Fig. 5(a)]. In each block, every pixel constitutes the same two types of those minerals. The minerals forming different blocks are not exactly the same. The abundance of the primary endmember in each pixel is not less than 95%, which guarantees better homogeneity of the ground object. The total variance of the simulated signal is

$$\sigma_s^2 = \sigma_{s\_1}^2 + \sigma_{s\_2}^2 + \cdots + \sigma_{s\_L}^2. \tag{20}$$

$\sigma_{s\_l}^2$ indicates the signal variance of the lth band, $l = 1, 2, \ldots, L$. The simulated noise is added to the simulated signal with a signal to noise ratio (SNR) of 20 dB

$$SNR(dB) = 10\log_{10}\left(\frac{\sigma_s^2}{\sigma_n^2}\right) \tag{21}$$

where σ_n^2 indicates the simulated noise's total variance. Thus

$$\sigma_n^2 = \sigma_s^2/[10\hat{}(SNR/10)]. \tag{22}$$

Every band from simulated noise is generated based on the same set of random numbers with a standard normal distribution. All the band variances from simulated noise follow a Gaussian shape centered at the band $L/2$

$$\sigma_{n\_l}^2 = \sigma_n^2 \frac{e^{-\frac{(l-L/2)^2}{2\eta^2}}}{\sum_{i=1}^{L} e^{-\frac{(i-L/2)^2}{2\eta^2}}}. \tag{23}$$

$\sigma_{n\_l}^2$ is the noise variance of the lth band. η controls the Gaussian curve's shape. In this study, $\eta = 90$. Because each band's variance of the simulated noise is different, the simulated noise is colored. Moreover, the random numbers located at two certain columns (columns 40 and 80) of the simulated noise are rearranged according to the simulated signal pixels' values at the same columns. Thus, there are two striping noise, and the simulated noise is correlated with the simulated signal. Finally, the simulated image is generated from simulated signal and simulated noise based on the image model (12). A real image covering Chengde district in Hebei Province of China was collected by Hyperion sensor (it is a hyperspectral imager carried by Earth-Observing-1 satellite by NASA) on November 14,

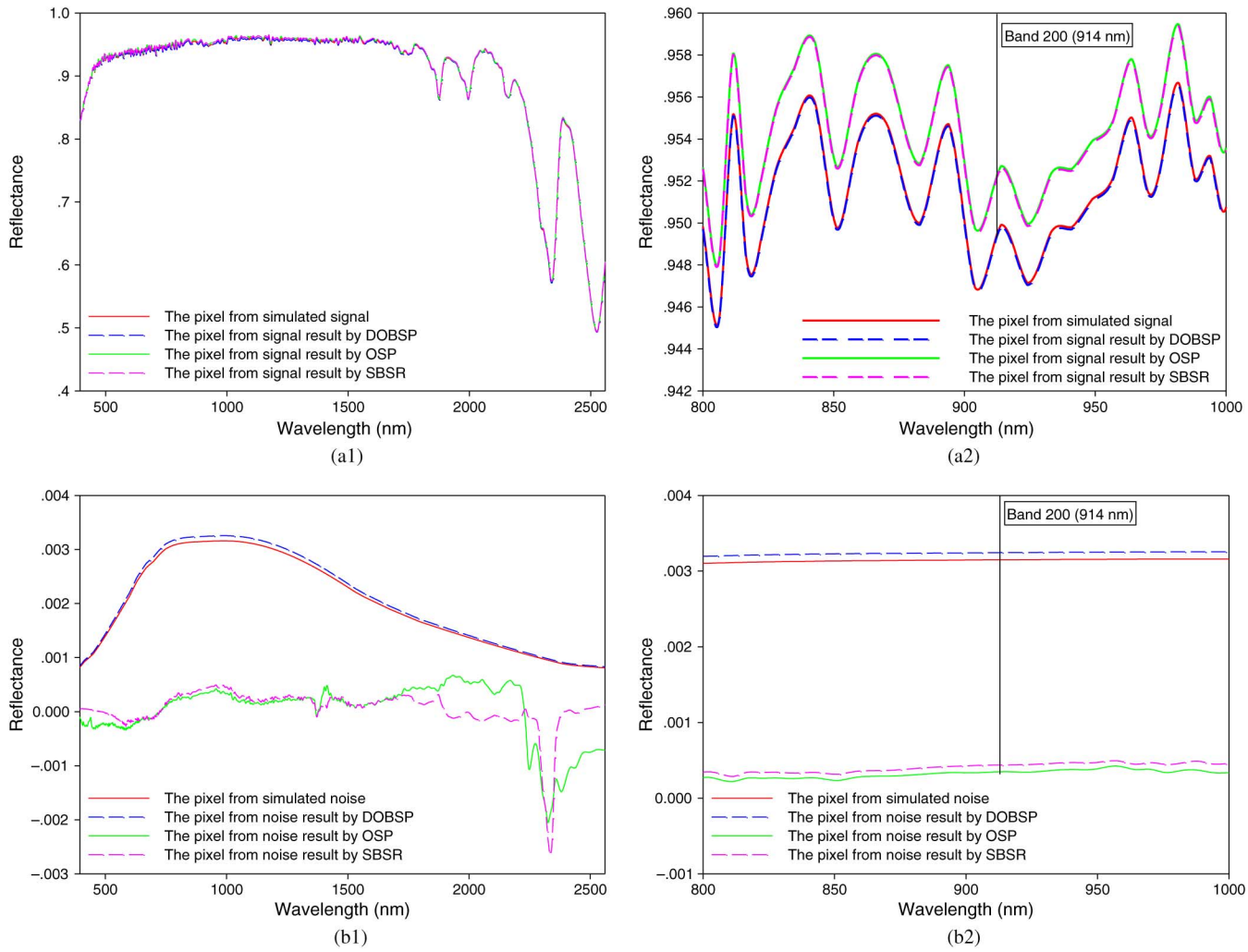

Fig. 9. Spectral curve of the boundary pixel at line 64 and column 96 from the signal and noise results. (a1) For signal result. (a2) Partial enlargement of (a1). (b1) For noise result. (b2) Partial enlargement of (b1).

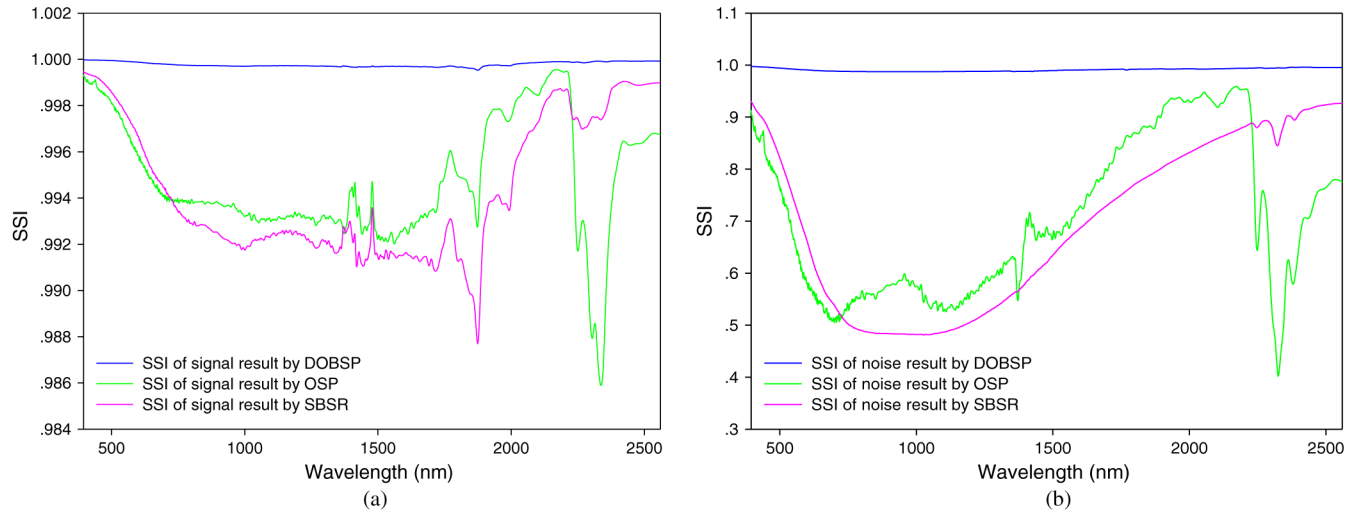

Fig. 10. SSI curve of the signal and noise results. (a) For signal result. (b) For noise result.

2002. A total of 114 bands were selected for the experiment (Table I). The image has been corrected by Fast Line-of-sight Atmospheric Analysis of Hypercubes (FLAASH). The Hyperion image contains striping noise and time-domain noise. To improve the computation speed, it was resized to 128 samples of 128 lines.

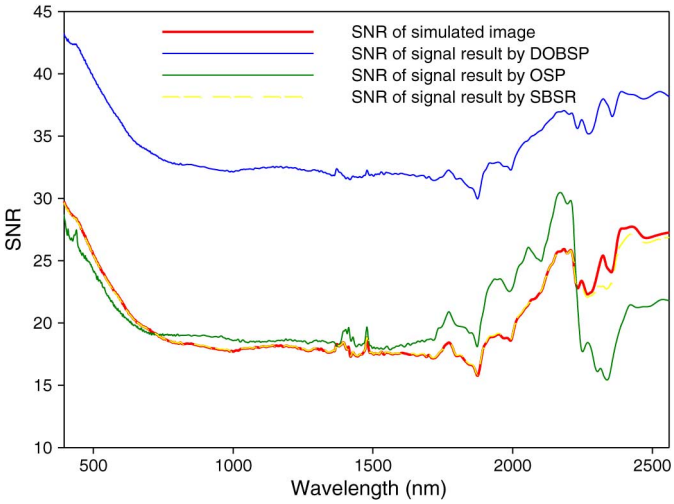

Fig. 11. SNR curve of the signal-band images.

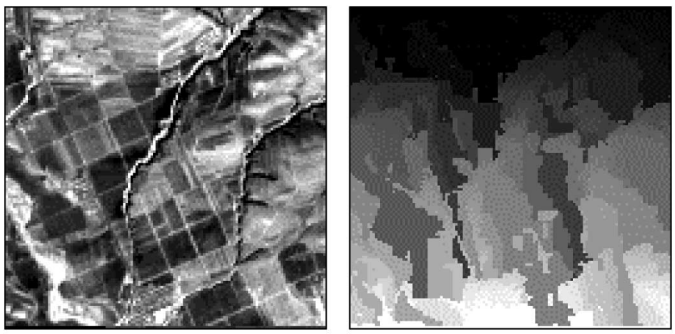

Fig. 12. Band 46 (813.48 nm) of the Hyperion image (a) and its segmented result (b).

III. Results and Discussion

For comparison purpose, the OSP and SBSR were introduced during the experiment. In the OSP, the noise is assumed independent on the signal. The SBSR algorithm uses a polynomial model to describe the relationship between the noise and signal. Moreover, both simulated and real Hyperion images were used to demonstrate the ability of DOBSP algorithm.

A. Simulated Image

Fig. 5(b) shows the segmented result using a spectral angle threshold of 0.05 radian. As can be seen, segmented image agrees with the spatial distribution of ground objects. The estimated signal and noise in each block are shown in Fig. 6. The signal estimates by SGLPF and GLPF look similar. However, GHPF failed to separate noise from signal on object boundaries. There are obvious boundaries existing in the noise estimated by GHPF, while little boundaries are included in the noise estimated by SGHPF. Moreover, the spectrum of the boundary pixel at line 64 and column 96, which is marked by a red square in Fig. 6(c2), was extracted for further investigation (Fig. 7). Both the signal and noise are well estimated by SGLPF and SGHPF respectively,

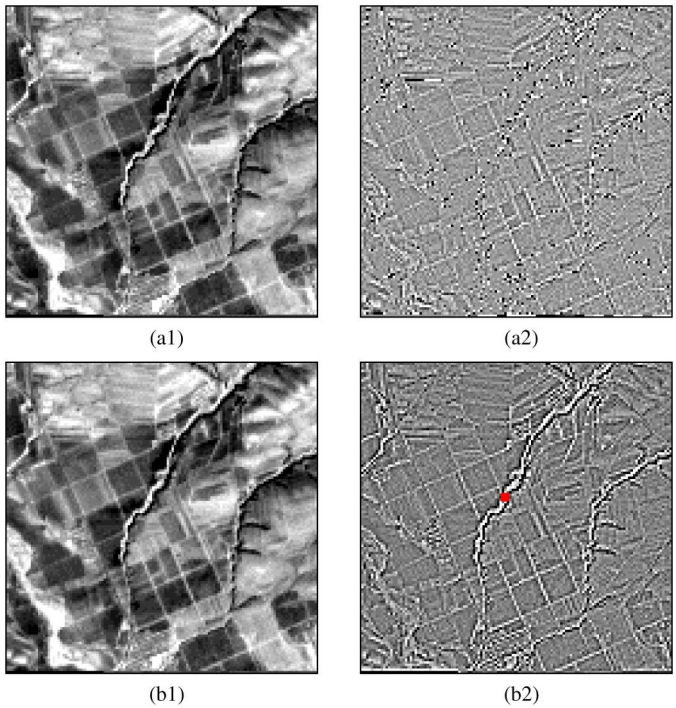

Fig. 13. Band 46 (813.48 nm) of the signal and noise estimates. (a1) Signal estimated by SGLPF. (a2) Noise estimated by SGHPF. (b1) Signal estimated by GLPF. (b2) Noise estimated by GHPF and the red square indicates the location of the texture pixel at line 55 and column 60.

with minor difference from the simulated signal and noise at this boundary pixel [Fig. 7(a1) and (a2)]. Compared with the signal estimated by SGLPF, the signal estimated by GLPF shows a larger difference with the simulated signal [Fig. 7(b1)]. The spectrum difference between the noise estimated by GHPF and the simulated noise is prominent at the boundary pixel [Fig. 7 (b2)].

In this experiment, the signal and noise are estimated by segmentation Gaussian filtering with great accuracy, thus there is little cross information between them. Moreover, the noise of each band was generated from the same set of random numbers with a given SNR. Hence, the first leading eigenvector of the noise estimate's covariance is adequate to be the basis vector of the noise subspace, while the signal subspace was represented by the first four principal components of the signal estimate. Their subspace angle was 0.34 radian (about 19.5°), which shows that the noise is closely related to the signal. In OSP, the first four principal components of the simulated image are used for computing signal subspace's projection matrix. The signal subspace's orthogonal complement projection matrix is regarded as the noise subspace's projection matrix. The signal and noise results of OSP are used as the signal and noise estimates in SBSR. The order of the polynomial in SBSR was set as 2.

Fig. 8 shows the signal and noise results obtained by DOBSP, OSP, and SBSR. The DOBSP gives a clearer signal image than OSP and SBSR. There are no apparent striping and time-domain noise in the signal image by DOBSP, compared with the signal images by OSP and SBSR. Noise images by DOBSP and OSP cannot be visually distinguished, while the noise image by SBSR has large deviation. With the spectrum of the boundary pixel at line 64 and column 96, it can be observed that DOBSP predicts

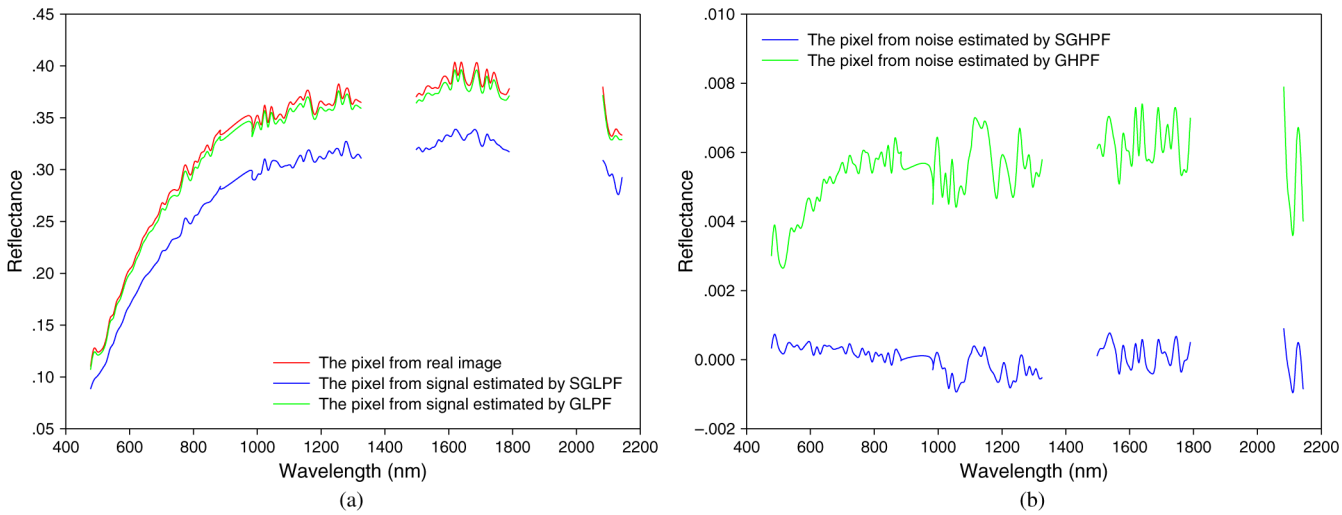

Fig. 14. Spectral curve of the texture pixel at line 55 and column 60 of signal and noise estimates. (a) For signal estimate. (b) For noise estimate.

the signal and noise more accurately than OSP and SBSR (Fig. 9). Because the signal and noise are estimated by OSP in the SBSR, the boundary pixel's spectrums from signal and noise results by SBSR are similar to those from signal and noise results by OSP. In addition, the structure similarity index (SSI) between the signal (noise) result and the simulated signal (noise) is computed (Fig. 10). SSI measures the similarity about luminance, contrast and structure between two images [40]. The closer to 1, the higher the similarity. As can be seen in Fig. 10, both SSI's of signal and noise images by DOBSP are closer to 1 than those of signal and noise images by OSP and SBSR. Hence, the DOBSP produces more accurate signal and noise results than OSP and SBSR. Moreover, the signal image obtained by DOBSP has higher SNR than those by OSP and SBSR (Fig. 11). Almost every band's SNR of the signal image obtained by DOBSP is larger than 30 dB while most the SNR's of bands in signal images by OSP and SBSR are smaller than 30 dB. The original simulated image's overall SNR is 20 dB. The overall SNR of the signal image by DOBSP is 34.239 dB which increases by 71.2%. The overall SNR's of the signal images by OSP and SBSR are just 20.106 and 20.003 dB, respectively. Both the OSP and SBSR barely improve the simulated image quality. The SBSR produced the worst noise result among the three algorithms.

B. Real Image

The segmented result of the real Hyperion image with the spectral angle threshold of 0.05 radian is shown in Fig. 12. Because the composition and distribution of real ground objects in real image are much more complicated than those in simulated image, each block includes fewer pixels to ensure its spectral homogeneity. Hence, segmented blocks donnot correspond to major boundaries in the real image obviously. However, these blocks agree with specific objects in the spectrum. The signal and noise estimates are shown in Fig. 13. The noise estimated by GHPF has more textures belonging to the signal than that estimated by SGHPF. For further investigation, the spectrum of a texture pixel at line 55 and column 60 is extracted and shown in Fig. 14. The spectral reflectance of the texture pixel from noise estimated by SGHPF is around 0. It complies with the general feature of noise. However, the spectral reflectance of the texture pixel from noise estimated by GHPF is much larger. Meanwhile, this texture pixel's spectral reflectance from signal estimated by GLPF is also larger than that from signal estimated by SGLPF. Moreover, compared with the texture pixel's spectrum from signal estimated by SGLPF, its spectrum from signal estimated by GLPF is much closer to the spectrum of the texture pixel from the original real image.

The segmented block is not completely homogenous due to the complexity of ground objects. Thus some textures that should belong to signal appear in the noise estimate. As a result, the first few principal components of the noise estimate contain some signal. Therefore, the 7th–114th principal components' eigenvectors of the noise estimate were chosen as the basis vectors of the noise subspace through visual inspection, while the first four principal components' eigenvectors of the signal estimate were used as the basis vectors of the signal subspace. The angle between the signal subspace and noise subspace is 1.55 radians (about 88.8°), indicating that they are not exactly orthogonal. The noise has some correlation with the signal in the Hyperion image. In OSP, the first four principal components' eigenvectors of the original image were used as the basis vectors of the signal subspace. The order of the polynomial in SBSR was also set as 2.

Figs. 15 and 16 show the signal and noise results by DOBSP, OSP, and SBSR. All the three algorithms produced signal images clearer than the original Hyperion image. However, the noise results obtained by these algorithms are different. There are some striping noise and time-domain noise in the band 19 of the original image. As can be seen in Fig. 15, the DOBSP extracts more effective striping noise than OSP. The noise image obtained by DOBSP contains fewer textures than that by OSP, while the noise image obtained by SBSR has obvious deviation. As shown in Fig. 16, band 46 of the original image mainly has time-domain noise. The noise image obtained by DOBSP has fewer textures than that by OSP. The noise image by SBSR is also inaccurate. The spectrum of the texture pixel at line 55 and column 60 is shown in Fig. 17. The texture pixel's spectrums from the signal images by DOBSP and OSP are very close but not the same. Compared with them, the texture pixel's spectrum from

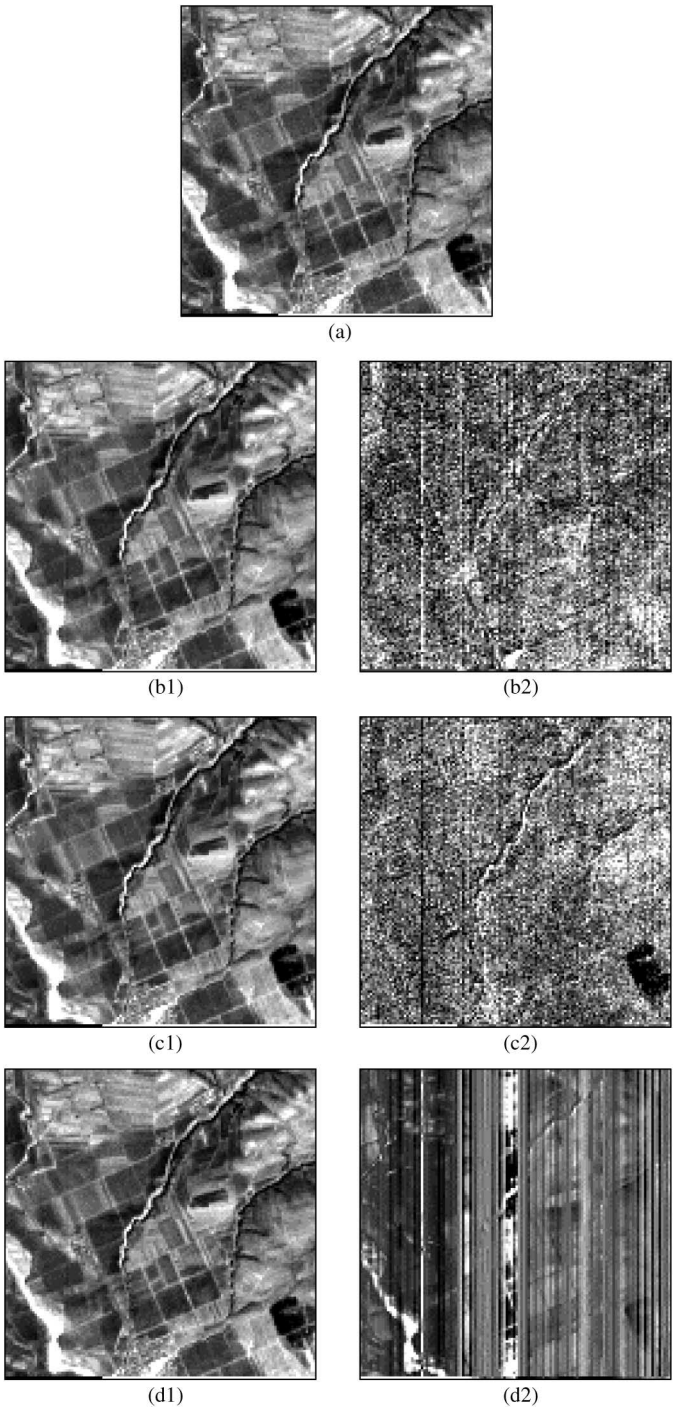

Fig. 15. Band 19 (538.74 nm) of the signal and noise results. (a) Original Hyperion image. (b1) Signal result by DOBSP. (b2) Noise result by DOBSP. (c1) Signal result by OSP. (c2) Noise result by OSP. (d1) Signal result by SBSR. (d2) Noise result by SBSR.

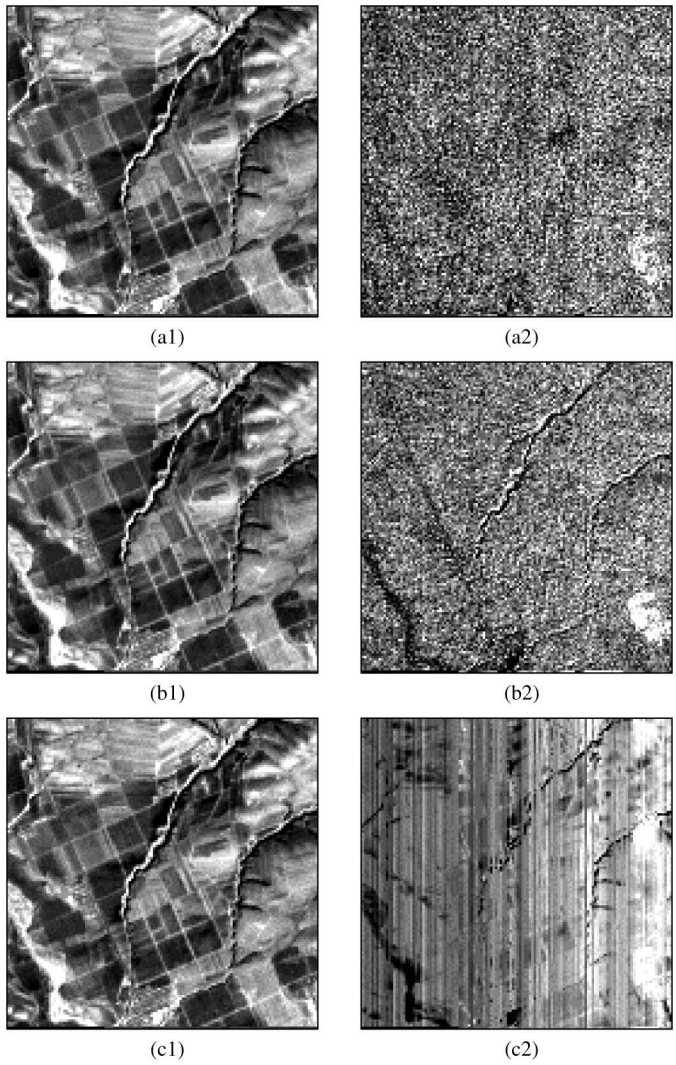

Fig. 16. Band 46 (813.48 nm) of the signal and noise results. (a1) Signal result by DOBSP. (a2) Noise result by DOBSP. (b1) Signal result by OSP. (b2) Noise result by OSP. (c1) Signal result by SBSR. (c2) Noise result by SBSR.

the signal image by SBSR is closer to that from the original image. Moreover, the texture pixel's spectrum from the noise image by SBSR is very different with those from the noise images by DOBSP and OSP. Though the real values of the signal and noise in real Hyperion image are unknown, the noise result by DOBSP which includes fewer textures should be more accurate than those by OSP and SBSR. That the noise result by DOBSP has higher accuracy confirms that the signal result by DOBSP also has higher reliability than those by OSP and SBSR from a side. In addition, the result by DOBSP doesnot have so much difference with the result by OSP as in the simulated image experiment. This is because the angle between the noise subspace and signal subspace is 19.5° in the simulated image experiment, while the subspace angle for the real image is 88.8°. The correlation between the noise and signal in the simulated image is much stronger than that in the real image. Hence, the difference between DOBSP and OSP in real image experiment is slighter than that in the simulated image experiment.

In both two experiments, segmentation Gaussian filtering obtained better signal and noise estimates than traditional Gaussian filtering, and the DOBSP produced better signal and noise results than OSP and SBSR. However, the accuracy of signal and noise estimates has a direct influence on the performance of DOBSP. To reduce the impact of image texture on the estimate, the image is firstly segmented into many homogeneous blocks based on a small spectral angle threshold. The smaller the

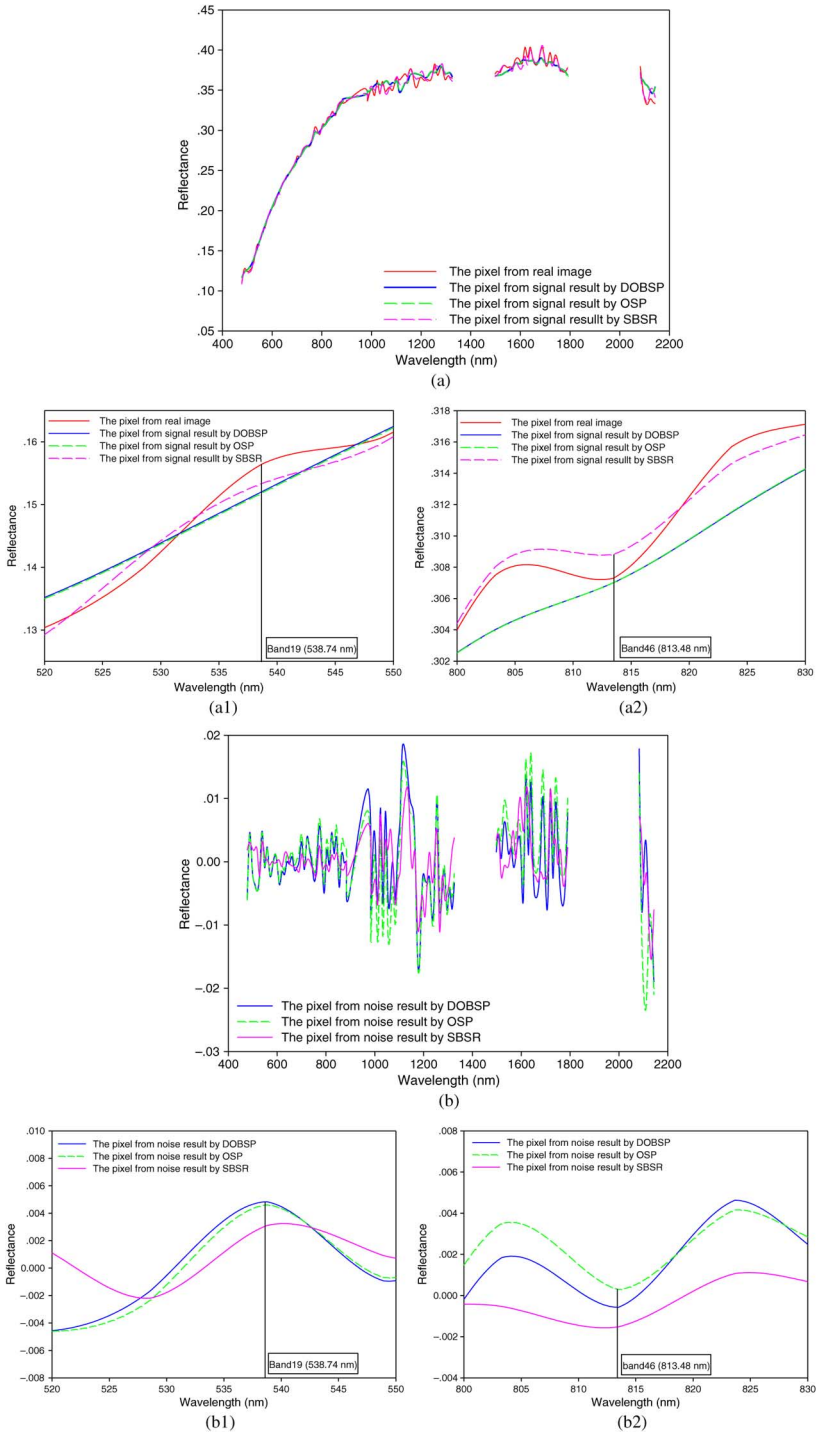

Fig. 17. Spectral curve of the pixel at line 55 and column 60 of signal and noise results. (a) For signal result. (a1) and (a2) are partial enlargements of (a). (b) For noise result. (b1) and (b2) are partial enlargements of (b).

spectral angle threshold, the more homogeneous the block, and the more accurate the estimate. But if the spectral angle threshold is too small, there may be only one pixel in the block, which will reduce the accuracy of the estimate significantly. Hence, setting a proper spectral angle threshold for image segmentation is important. Furthermore, it cannot guarantee every block to be completely homogeneous even if the spectral angle threshold is small, because the composition and distribution of the actual ground objects are usually very complicated. Thus, some spectral differences caused by nonuniformity of ground objects in a block may be estimated as noise mistakenly. Then the inaccurate estimates can affect subspace identification. Some noise's components may include signal information and some signal's components may contain noise information after PCA on noise and signal estimates, which may have influence on the selection of basis vectors for subspace. Inaccurate basis vectors will lead to wrong oblique projection matrices, and thus generate incorrect results.

IV. Conclusion

In this paper, a new denoising algorithm named DOBSP has been proposed. It is based on OBSP, which considers the correlation between the signal and noise. The algorithm consists of three main steps. It first estimates the signal and noise through segmentation Gaussian filtering, which reduces more influence of the image texture than traditional Gaussian filtering does. Then, the signal and noise estimates are fed into PCA to identify their respective subspaces. The basis vectors of subspace are chosen from eigenvectors of estimate's covariance matrix by visual inspecting the corresponding component images after PCA. Finally, two OBSP matrices are computed from basis vectors, and the signal and noise are extracted from the original image through OBSP. To assess the DOBSP algorithm, both simulated and real Hyperion images were used in experiments. The OSP and SBSR algorithms were introduced for comparison. Both signal and noise results obtained by DOBSP on the simulated image are closer to the original simulated signal and noise than those by OSP and SBSR, and the SNR of the signal result by DOBSP improves significantly. The noise result obtained by DOBSP on the Hyperion image has fewer textures than that by OSP, while the noise result obtained by SBSR shows large deviation. Moreover, the more accurate noise result extracted by DOBSP on the Hyperion image proves that the signal result by DOBSP is more reliable than those by OSP and SBSR from the side.

Acknowledgment

The authors acknowledge the support from Hyperspectral Remote Sensing Laboratory, China Academy of Sciences. They would like to thank Prof. C.-I. Chang from Remote Sensing Signal and Image Processing Laboratory, University of Maryland, Baltimore County (UMBC), USA, and Prof. M. Song from Information and Technology College, Dalian Maritime University, China, for providing useful suggestions. They also would like to thank the reviewers for their valuable comments which have resulted in a number of improvements in the paper.

References

[1] A. F. H. Goetz, G. Vane, J. E. Solomon, and B. N. Rock, "Imaging spectrometry for earth remote-sensing," *Science*, vol. 228, pp. 1147–1153, 1985.

[2] A. F. H. Goetz, "Hyperspectral imaging and quantitative remote sensing," in *Proc. Land Satellite Information in the Next Decade*, 1995, pp. E1–E10.

[3] A. F. H. Goetz, "Three decades of hyperspectral remote sensing of the earth: A personal view," *Remote Sens. Environ.*, vol. 113, pp. S5–S16, 2009.

[4] Q. Tong, Y. Xue, and L. Zhang, "Progress in hyperspectral remote sensing science and technology in China over the past three decades," *IEEE J. Sel. Topics Appl. Earth Observ. Remote Sens.*, vol. 7, no. 1, pp. 70–91, Jan. 2014.

[5] B. Aiazzi *et al.*, "Noise modelling and estimation of hyperspectral data from airborne imaging spectrometers," *Ann. Geophys.*, vol. 49, pp. 1–9, 2006.

[6] L. Gao, B. Zhang, X. Zhang, and Q. Shen, "Study on the method for estimating the noise in remote sensing images based on local standard deviations," *J. Remote Sens.*, vol. 11, pp. 201–208, 2007.

[7] P. Toivanen, A. Kaarna, J. Mielikainen, and M. Laukkanen, "Noise reduction methods for hyperspectral images," in *Image and Signal Processing for Remote Sensing Viii*, vol. 4885, S. B. Serpico, Ed. Bellingham, WA, USA: SPIE Int. Soc. Opt. Eng., 2003, pp. 307–313.

[8] Y. Qian and M. Ye, "Hyperspectral imagery restoration using nonlocal spectral-spatial structured sparse representation with noise estimation," *IEEE J. Sel. Topics Appl. Earth Observ. Remote Sens.*, vol. 6, no. 2, pp. 499–515, Apr. 2013.

[9] L. Gao and Q. Du, "A comparative study on linear regression-based noise estimation for hyperspectral imagery," *IEEE J. Sel. Topics Appl. Earth Observ. Remote Sens.*, vol. 6, no. 2, pp. 488–498, Apr. 2013.

[10] P. Latorre-Carmona, J. Martinez Sotoca, F. Pla, J. Bioucas-Dias, and C. J. Ferre, "Effect of denoising in band selection for regression tasks in hyperspectral datasets," *IEEE J. Sel. Topics Appl. Earth Observ. Remote Sens.*, vol. 6, no. 2, pp. 473–481, Apr. 2013.

[11] J. Wang, Y. Wang, and C. Li, "Noise model of hyperspectral imaging system and influence on radiation sensitivity," *J. Remote Sens.*, vol. 14, pp. 607–620, 2010.

[12] C. I. Chang, "Orthogonal subspace projection (OSP) revisited: A comprehensive study and analysis," *IEEE Trans. Geosci. Remote Sens.*, vol. 43, no. 3, pp. 502–518, Mar. 2005.

[13] C. I. Chang, W. Xiong, H. M. Chen, and J. W. Chai, "Maximum orthogonal subspace projection approach to estimating the number of spectral signal sources in hyperspectral imagery," *IEEE J. Sel. Topics Signal Process.*, vol. 5, no. 3, pp. 504–520, Jun. 2011.

[14] Q. Du, H. Ren, and C. I. Chang, "A comparative study for orthogonal subspace projection and constrained energy minimization," *IEEE Trans. Geosci. Remote Sens.*, vol. 41, no. 6, pp. 1525–1529, Jun. 2003.

[15] J. C. Harsanyi, "*Detection and classification of subpixel signatures in hyperspectral image sequences*," Ph. D. dissertation, Dept. Comput. Sci. Electr. Eng., Univ. Maryland, Baltimore, MD, USA, 1993.

[16] C. I. Chang and Q. Du, "An interference rejection approach to noise adjusted principal components transform," in *Proc. IEEE Int. Geosci. Remote Sens. Symp. (IGARSS)—Sens. Manag. Environ.*, 1998, vol. 1–5, pp. 2059–2061.

[17] C. I. Chang and Q. Du, "Interference and noise-adjusted principal components analysis," *IEEE Trans. Geosci. Remote Sens.*, vol. 37, no. 5, pp. 2387–2396, Sep. 1999.

[18] Q. Du, "Interference and noise adjusted principal components analysis for hyperspectral image compression," in *Chemical and Biological Standoff Detection II*, vol. 5584, J. O. Jensen and J. M. Theriault, Eds. Bellingham, WA, USA: SPIE Int. Soc. Opt. Eng., 2004, pp. 186–193.

[19] Q. Du and N. Raksuntorn, "Hyperspectral image analysis using noise-adjusted principal component transform," in *Algorithms and Technologies for Multispectral, Hyperspectral, and Ultraspectral Imagery XII Pts 1 and 2*, vol. 6233, S. S. Shen and P. E. Lewis, Eds., Bellingham, WA, USA: SPIE Int. Soc. Opt. Eng., 2006 pp. F2330–F2330.

[20] Q. Du and H. Szu, "Interference and noise adjusted principal components analysis for hyperspectral remote sensing image compression," in *Independent Component Analyses, Wavelets, Unsupervised Smart Sensors, and Neural Networks IV*, vol. 6247, H. H. Szu Ed., Bellingham, WA, USA: SPIE Int. Soc. Opt. Eng., 2006 pp. A2470–A2470.

[21] R. E. Roger, "Principal components transform with simple, automatic noise adjustment," *Int. J. Remote Sens.*, vol. 17, pp. 2719–2727, 1996.

[22] B. Xu and P. Gong, "Noise estimation in a noise-adjusted principal component transformation and hyperspectral image restoration," *Can. J. Remote Sens.*, vol. 34, pp. 271–286, Jun. 2008.

[23] A. Dadon, E. Ben-Dor, and A. Karnieli, "Use of derivative calculations and minimum noise fraction transform for detecting and correcting the spectral curvature effect (smile) in hyperion images," *IEEE Trans. Geosci. Remote Sens.*, vol. 48, no. 6, pp. 2603–2612, Jun. 2010.

[24] C. Gordon, "A generalization of the maximum noise fraction transform," *IEEE Trans. Geosci. Remote Sens.*, vol. 38, no. 1, pp. 608–610, Jan. 2000.

[25] A. A. Nielsen, "Kernel maximum autocorrelation factor and minimum noise fraction transformations," *IEEE Trans. Image Process.*, vol. 20, no. 3, pp. 612–624, Mar. 2011.

[26] L. Alparone, M. Selva, B. Aiazzi, S. Baronti, F. Butera, L. Chiarantini, "Signal-dependent noise modelling and estimation of new-generation imaging spectrometers," in *Proc. 1st Workshop Hyperspectral Image Signal Process.: Evol. Remote Sens. (WHISPERS'09)*, Grenoble, France, Aug. 2009, pp. 364–367.

[27] B. Aiazzi *et al.*, "Hyperspectral noise modelling and estimation," in *Proc. Hyperspectral Workshop*, 2010, pp. 17–19.

[28] N. Acito, M. Diani, and G. Corsini, "Subspace-based striping noise reduction in hyperspectral images," *IEEE Trans. Geosci. Remote Sens.*, vol. 49, no. 4, pp. 1325–1342, Apr. 2011.

[29] G. Corsini, M. Dian, and T. Walzer, "Striping removal in MOS-B data," *IEEE Trans. Geosci. Remote Sens.*, vol. 38, no. 3, pp. 1439–1446, May 2000.

[30] R. C. Gonzalez and R. E. Woods, *Digital Image Processing*, 2nd ed., Beijing, China: Publishing House of Electronics Industry, 2009.

[31] D. Zhang, *Digital Image Processing Using MatLab*. Beijing, China: Posts & Telecom Press, 2009.

[32] J. Harsanyi, W. Farrand, and C.-I. Chang, "Determining the number and identity of spectral endmembers: An integrated approach using Neyman–Pearson eigenthresholding and iterative constrained RMS error minimization," in *Proc. 9th Thematic Conf. Geologic Remote Sens.*, 1993, pp. 395–408.
[33] H. V. Poor, *An Introduction to Detection and Estimation Theory*, 2nd ed. NewYork, NY, USA: Springer, 1994.
[34] C. I. Chang and Q. Du, "Estimation of number of spectrally distinct signal sources in hyperspectral imagery," *IEEE Trans. Geosci. Remote Sens.*, vol. 42, no. 3, pp. 608–619, Mar. 2004.
[35] P. A. Wedin, "On angles between subspaces of a finite dimensional inner product space," in *Matrix Pencils, Lecture Notes in Mathematics*, vol. 973, B. Kagstrom and A. Ruhe, Eds. New York, NY, USA: Springer, 1983, pp. 263–285.
[36] A. Bjorck and G. Golub, "Numerical methods for computing angles between linear subspaces," *Math. Comput.* vol. 27, pp. 579–594, 1973.
[37] Y. Cheng, K. Zhang, and Z. Xu, *Theory of Matrix*, 3rd ed. Xi'an, China: Northwestern Polytechnic Univ. Press, 2006.
[38] R. T. Behrens and L. L. Scharf, "Signal processing applications of oblique projection operators," *IEEE Trans. Signal Process.*, vol. 42, no. 6, pp. 1413–1424, Jun. 1994.
[39] R. T. Behrens and L. L. Scharf, "Corrections to signal processing applications of oblique projection operators," *IEEE Trans. Signal Process.*, vol. 44, no. 5, p. 1300, May 1996.
[40] Z. Wang, A. C. Bovik, H. R. Sheikh, and E. P. Simoncelli, "Image quality assessment: from error visibility to structural similarity," *IEEE Trans. Image Process.*, vol. 13, no. 4, pp. 600–612, Apr. 2004.

Qian Wang received the B.E. degree in earth information science and technology from the Department of Earth Sciences and Resources, China University of Geosciences, Beijing, China, in 2007, the M.E. degree in earth detection and information technology from the Department of Earth Sciences and Resources, China University of Geosciences, Beijing, China, in 2010. Currently, she is pursuing the Ph.D. degree in the Institute of Remote Sensing and Digital Earth, Chinese Academy of Sciences, Beijing, China.

Her research interests include hyperspectral image processing algorithm and weak information extraction from hyperspectral image.

Lifu Zhang (S'04–M'05) received the B.E. degree in photogrammetry and remote sensing from the Department of Airborne Photogrammetry and Remote Sensing, Wuhan Technical University of Surveying and Mapping(WTUSM), Wuhan, China, in 1992, the M.E. degree in photogrammetry and remote sensing from the State Key Laboratory of Information Engineering in Surveying, Mapping and Remote Sensing, WTUSM, Wuhan, China, in 2000, and the Ph.D. degree in photogrammetry and remote sensing from the State Key Laboratory of Information Engineering in Surveying, Mapping and Remote Sensing, Wuhan University, Wuhan, China, in 2005.

He was a Visiting Researcher with the Department of Information and Computer Sciences, Nara Women's University, Nara, Japan, from 2003 to 2004, a Postdoctoral Researcher with the Institute of Remote Sensing and Geographic Information System, School of Earth and Space Sciences, Peking University, Beijing, China, from 2005 to 2007, and an Advanced Visiting Researcher with the Earth Science and Resource Engineering, Commonwealth Scientific and Industrial Research Organization (CSIRO), Sydney, Australia, in 2011. In 2007, he joined the former Institute of Remote Sensing Applications (IRSA), Chinese Academy of Sciences (CAS), Beijing, China, where he was a research professor and a scientist team leader. From November 2012, IRSA was merged with Institute of Remote Sensing and Digital Earth (RADI), where, he is a Professor and the Head of the Hyperspectral Remote Sensing Laboratory, RADI , CAS. His research interests include hyperspectral remote sensing, imaging spectrometer system development and its applications.

Dr. Zhang is a member of SPIE and the Academy of Space Science of China. He is also a Committeeman of Chinese National Committee of the International Society for Digital Earth (CNISDE), a Vice Chairman of hyperspectral earth observation committee (HEOC) of CNISDE, and a Standing Committeeman of the Expert Committee of China Association of Remote Sensing Applications.

Qingxi Tong received the B.S. degree in agrometeorology from Odessa of Hydrometeorological Institute, Odessa, Ukraine.

He has been engaged in the study on the development and application of remote sensing since the beginning of 1970. Currently, he is the Chief Scientist in a cooperation project of the National Remote Sensing Center of China (NRSCC), Beijing, China, and the Surrey Space Centre of Surrey University, Surrey, U.K., for the development of a small satellite. He serves as the Chairman of the Expert Committee of NRSCC, the Ministry of Science and Technology of China. As a result, a high-performance small satellite named "Beijing-1" has been launched and successfully operated. He is one of the Principal Scientists in remote sensing in China. He has made outstanding contribution in the development of remote sensing technology and applications, particularly in the development of airborne remote sensing system, and in the study of remote sensing spectral properties of Earth resources and environments and the development of hyperspectral remote sensing in China as well. He is an Associate Editor of *Journal of Remote Sensing*, and an Editorial Committeeman of *Chinese Journal of Space Science*. He is also active in the international cooperation.

Prof. Tong was a recipient of the National Prizes for Progress of Science and Technology and the Chinese Academy of Sciences (CAS) Prize for Progress of Science and Technology many times due to his achievements. He was also a recipient of the "Achievement for International Remote Sensing Science & Technology" by the SPIE in 2002. He was elected as a Member of CAS in 1997 and an Academician of the International Eurasian Academy of Sciences in the same year.

Feizhou Zhang received the B.E. degree in industry electric automation from the Department of Electronic and Electric Engineering, Shanxi Technology College, Xi'an, China, in 1986, the M.E. and Ph.D. degrees in navigation, control, and guide, School of Automatic Science, University of Aeronautics and Astronautics (BUAA), Beijing, China, in1997 and 2001, respectively.

He is currently an Associate Professor and the Vice Dean with the School of Earth and Spatial Sciences, Peking University, Beijing, China. His research interests include satellite navigation, internet of things, software receiver, ITS and spatial information integration, etc. He has published more than 100 papers among which over 70 are indexed by SCI and EI.